



Bergische Universität Wuppertal

Fakultät für Mathematik und Naturwissenschaften

Institute of Mathematical Modelling, Analysis and Computational Mathematics (IMACM)

Preprint BUW-IMACM 23/10

F. Klass and A. Gabbana and A. Bartel

## **Characteristic Boundary Condition for Thermal Lattice Boltzmann Methods**

July 10, 2023

<http://www.imacm.uni-wuppertal.de>



# Characteristic Boundary Condition for Thermal Lattice Boltzmann Methods

Friedemann Klass<sup>a</sup>, Alessandro Gabbana<sup>b</sup> and Andreas Bartel<sup>a</sup>

<sup>a</sup>University of Wuppertal, Gausstrasse 20, Wuppertal, 42119, Germany

<sup>b</sup>Eindhoven University of Technology, Eindhoven, 5600 MB, The Netherlands

## ARTICLE INFO

**Keywords:**

CFD

Non-reflective Boundary Conditions

Characteristic Boundary Condition

Locally One-Dimensional Inviscid

Thermal flows

High order lattice Boltzmann methods

## ABSTRACT

We introduce a non-reflecting boundary condition for the simulation of thermal flows with the lattice Boltzmann Method (LBM). We base the derivation on the locally one-dimensional inviscid analysis, and define target macroscopic values at the boundary aiming at minimizing the effect of reflections of outgoing waves on the bulk dynamics. The resulting macroscopic target values are then enforced in the LBM using a mesoscopic Dirichlet boundary condition. We present a procedure which allows to implement the boundary treatment for both single-speed and high order multi-speed LBM models, by conducting a layerwise characteristic analysis. We demonstrate the effectiveness of our approach by providing qualitatively and quantitative comparison of several strategies for the implementation of an open boundary condition in standard numerical benchmarks. We show that our approach allows to achieve increasingly high accuracy by relaxing transversal and viscous terms towards prescribed target values.

## 1. Introduction

In many numerical simulations the physical domain of a given problem is infeasibly large and only information about a small region of interest, encapsulated in the physical domain, is required. In these situations, the computational domain can be obtained by truncating the original domain. This gives rise to artificial boundaries that need to be treated using a boundary condition (BC). Since these artificial boundaries should not interact with the bulk dynamics, it is beneficial to employ non-reflecting boundary conditions (NRBC), which let waves crossing the boundary out of the computational domain without causing reflection effects.

The so-called characteristic boundary condition (CBC) is among the most popular choices for NRBC. Its working principle consists of identifying incoming and outgoing waves at the boundary, to then modulate amplitude variations of incoming waves. The CBC was originally developed for nonlinear hyperbolic systems [1, 2] and later extended to the Navier-Stokes equations [3], where it is widely used in the area of computational aero-acoustics [4, 5]. Furthermore, CBCs have been successfully applied to magneto-hydrodynamics [6, 7], reacting [8] and turbulent flow in two [9] and three [10] spatial dimensions.

In this work, we present the derivation of a CBC for thermal compressible flows, modeled by the Navier-Stokes-Fourier equations. We employ the lattice Boltzmann method (LBM) for the time evolution of the fluid bulk dynamic. The LBM is an established algorithm for the simulation of fluid flows that can be derived as a systematic approximation of the Boltzmann equation [11, 12]. It has gained a lot of popularity due to its simple algorithmic structure, which makes it highly

amenable to large scale parallelization [13, 14, 15], the ability to handle complex geometries [16] as well as multi-phase [17] and multi-component [18] flows. Stemming from the kinetic layer, the LBM provides the description of a fluid flow in terms of a discrete set of particle distribution functions (populations) sitting at the sites of a discrete lattice, with the macroscopic behavior emerging from the velocity moments of the distribution. Continuous efforts are being made to extend the range of applicability of LBM and tackle problems such as thermal compressible flows. There are three main approaches to thermal LBM present in literature: i) hybrid coupling with a macroscopic solver (e.g. finite differences, or finite volume) for evolving the energy equation [19], ii) the double distribution approach, where a second set of populations is used to evolve the temperature field [20] and iii) models based on high order quadrature rules [11, 21]. The latter approach provides an elegant and self-consistent kinetic description of thermal compressible flow [22, 23] via the high order moments of the particle distribution function. However, higher order models give rise to multi-speed velocity stencils, i.e., discrete velocity stencils with a maximum displacement greater than one, which generally complicate the definition of boundary conditions.

Few implementations of characteristic boundary conditions for isothermal (single-speed) LBM have been reported in the literature [24, 25, 26, 27], finding application in the simulation of fluid flows in high Reynolds number regimes [28, 29, 30]. To the best of our knowledge, there are currently only two works in the literature where the application of characteristic BCs for multi-speed LBM is discussed: the CBC for the Navier-Stokes equations presented in [24] has been used in conjunction with multi-speed velocity stencils in a previous article [31] by the authors of the work at hand, and recently multi-speed CBC was used in the context

\*Corresponding author

✉ klass@math.uni-wuppertal.de (F. Klass)

ORCID(s): 0000-0002-8566-0918 (F. Klass); 0000-0002-8367-6596 (A. Gabbana); 0000-0003-1979-179X (A. Bartel)

of thermo-acoustic problems governed by the Euler equations [32].

In the work at hand, we develop a CBC suitable for thermal compressible flows governed by the Navier-Stokes-Fourier equations. We will focus our analysis on its coupling with multi-speed LBM, however we shall remark that the procedure here described is general and can be employed also in combination to the other approaches for thermal LBM listed above.

This article is organized as follows: Sec. 2 provides a brief description of the LBM scheme used in this work. In Sec. 3, we present the derivation of a CBC for the Navier-Stokes-Fourier equations as well as a simplified version where transversal and viscous terms are discarded. We then provide details on how to couple the macroscopic BC with the mesoscopic layer. Subsequently, in Sec. 4, we benchmark the numerical accuracy of the BC in several test-beds, comparing different realization of the CBC with a simple zero-gradient extrapolation. Finally, concluding remarks and future directions are summarized in Sec. 5.

## 2. Thermal Lattice Boltzmann Method

In this section, we provide a succinct overview of the LBM which we use in this work to solve the Navier-Stokes-Fourier equations. The reader not familiar with LBM is referred to Ref. [33, 34] for a more comprehensive introduction. We remark that while we focus on  $d = 2$  spatial dimensions during this work, to ease the presentation and provide a broad and comprehensive picture of the behavior of CBCs, the generalization to three spatial dimensions is conceptually straightforward (see Appendix A).

The LBM operates at the mesoscopic level and provides the time evolution of a fluid flow via the synthetic dynamics of a set of discrete velocity distribution functions, governed by the discrete lattice Boltzmann equation: (for  $i = 1, \dots, q$ )

$$f_i(\mathbf{x} + \mathbf{c}_i \Delta t, t + \Delta t) = f_i(\mathbf{x}, t) + \Omega_i(\mathbf{x}, t). \quad (1)$$

In the above,  $f_i(\mathbf{x}, t)$  are the discrete single particle distribution functions (to which we will refer to as lattice populations), defined at each node  $\mathbf{x}$  of a Cartesian grid, and corresponding to each of the  $q$  components of a velocity stencil  $\{\mathbf{c}_i = (c_{i,x}, c_{i,y}) : i = 1, \dots, q\}$ , while  $\Omega_i$  is the collision operator.

Hydrodynamic quantities of interest, such as density  $\rho$ , velocity  $\mathbf{u} = (u_x, u_y)^\top$  and temperature  $T$  can be calculated from the velocity moments of the distribution:

$$\rho = \sum_{i=1}^q f_i, \quad \rho \mathbf{u} = \sum_{i=1}^q f_i \mathbf{c}_i, \quad 2\rho T = \sum_{i=1}^q f_i |\mathbf{c}_i - \mathbf{u}|^2. \quad (2)$$

In Eq. (2), equality holds if the lattice velocities are chosen according to the abscissa of a sufficiently high-order Gauss-Hermite quadrature [35] i.e.,  $\{(\omega_i, \mathbf{c}_i) : i = 1, \dots, q\}$ , where  $\omega_i$  are the quadrature weights. It is customary to distinguish between different LBMs using the  $DdQq$  nomenclature, in which  $d$  refers to the number of spatial dimensions and  $q$  to the number of discrete components.

The commonly adopted D2Q9 model correctly recovers density and velocity, its underlying quadrature is not sufficiently accurate to capture also the temperature. For this reason, in this work, we employ the D2Q17 and the D2Q37 velocity stencils (see Fig. 1); while both models can correctly recover the third order velocity moments of the particle distribution function, it can be shown [11] that the D2Q17 stencil fails to capture the non-equilibrium component of the heat-flux  $\mathbf{q}$ ,

$$\mathbf{q} = \frac{1}{2} \sum_{i=1}^q f_i |\mathbf{c}_i - \mathbf{u}|^2 (\mathbf{c}_i - \mathbf{u}), \quad (3)$$

a flaw cured by the D2Q37 stencil.

The collision operator  $\Omega_i$  is often modeled with the single relaxation time Bhatnagar-Gross-Krook (BGK) approximation [36],

$$\Omega_i = -\frac{1}{\tau} (f_i(\mathbf{x}, t) - f_i^{\text{eq}}(\mathbf{x}, t)), \quad (4)$$

consisting of a relaxation with relaxation time  $\tau$  towards a local equilibrium  $f_i^{\text{eq}}$ , which is defined as expansion in Hermite polynomials of the Maxwell-Boltzmann distribution. In this work, we consider a third order expansion for the D2Q17 stencil,

$$f_i^{\text{eq},3}(\rho, \mathbf{u}, T) = \omega_i \rho \left( 1 + \mathbf{u} \cdot \mathbf{c}_i + \frac{1}{2c_s^2} [(\mathbf{u} \cdot \mathbf{c}_i)^2 - u^2 + (T-1)(c_i^2 - 2)] + \frac{\mathbf{u} \cdot \mathbf{c}_i}{6c_s^4} [(\mathbf{u} \cdot \mathbf{c}_i)^2 - 3u^2 + 3(T-1)(c_i^2 - 4)] \right), \quad (5)$$

and a fourth order expansion for the D2Q37 stencil

$$f_i^{\text{eq},4}(\rho, \mathbf{u}, T) = f_i^{\text{eq},3}(\rho, \mathbf{u}, T) + \omega_i \rho \left( \frac{1}{24c_s^6} [(\mathbf{u} \cdot \mathbf{c}_i)^4 - 6(\mathbf{u} \cdot \mathbf{c}_i)^2 u^2 + 3u^4 + 6(T-1)((\mathbf{u} \cdot \mathbf{c}_i)^2 (c_i^2 - 4) + |\mathbf{u}|^2 (4 - c_i^2)) + 3(T-1)^2 (c_i^4 - 8c_i^2 + 8)] \right), \quad (6)$$

respectively, where  $u^2 = \mathbf{u} \cdot \mathbf{u}$ ,  $c_i^2 = \mathbf{c}_i \cdot \mathbf{c}_i$  and the speed of sound  $c_s$  is a lattice specific constant. The values of the lattice weights  $\omega_i$  and speed of sound for both stencils are given in Appendix B.

By applying a multiscale Chapman-Enskog expansion, see [37], it can be shown [23] that Eq. (1) delivers a second order approximation of the macroscopic Navier-Stokes-Fourier equations. In the absence of external forces, they can be stated as

$$D_t \rho = -\rho \partial_i u_i \\ \rho D_t u_i = -\partial_i P + \mu \partial_{jj} u_i + \left( 1 - \frac{1}{c_v} \right) \mu \partial_i \partial_j u_j \quad (7)$$





the time evolution of  $\mathbb{U}$  vanishes [1, 2]. In other words, this means no information enters the bulk and the influence of external dynamics on the domain of interest is completely suppressed.

In the LODI approximation (Eq. (10)), this translates to setting incoming wave amplitude variations to zero, i.e., we substitute  $\mathcal{L}_x$  with a vector  $\bar{\mathcal{L}}_x$ , whose  $i$ -th component is defined as

$$\bar{\mathcal{L}}_{x,i} = \begin{cases} \mathcal{L}_{x,i} & \text{for an outgoing wave } i, \\ 0 & \text{for an incoming wave } i. \end{cases} \quad (12)$$

By contrast, in the CBC approach, setting incoming wave amplitudes to zero will not guarantee that no information will travel from the boundary to the bulk domain for cases where transversal and viscous contributions are relevant to the dynamic. This can be seen by casting Eq. (11) in the following form:

$$\frac{\partial \mathbb{U}}{\partial t} = -S^{-1} \bar{\mathcal{L}}_x + \mathbb{T} + \mathbb{V} = -S^{-1} (\bar{\mathcal{L}}_x - \mathcal{T}_x - \mathcal{V}_x),$$

where  $\mathcal{T}_x = S\mathbb{T}$ ,  $\mathcal{V}_x = S\mathbb{V}$ .

As a remedy, the contributions  $\mathcal{T}_x$  and  $\mathcal{V}_x$  can be absorbed in the unknown wave amplitude variation  $\bar{\mathcal{L}}_{x,i}$  as proposed in Ref. [27]:

$$\bar{\mathcal{L}}_{x,i} = \mathcal{T}_{x,i} + \mathcal{V}_{x,i}. \quad (13)$$

This strategy of completely annihilating incoming waves theoretically leads to a perfectly non-reflecting BC. In practice, however, due to discretization errors and the fact that wave amplitudes get computed from an approximate system, reflection waves are generally still present.

*B) Relaxation toward target quantities.* As observed in the previous paragraph, posing a perfectly non-reflecting BC gives no control over the macroscopic values at the boundary since their time evolution strongly depends on the outgoing waves. On the other hand, imposing desired target values by means of a Dirichlet BC generally leads to significant reflection waves. As a trade-off between these two cases, a relaxation towards a target macroscopic value can be incorporated in the incoming wave amplitude variations [3, 38]. A general expression for the unknown wave amplitudes in conjunction with the CBC approach was proposed in Ref. [8] and reads as:

$$\bar{\mathcal{L}}_{x,i} = \mathcal{T}_{x,i} + \mathcal{V}_{x,i} + \alpha(\mathcal{T}_{x,i}^{\text{ex}} - \mathcal{T}_{x,i}) + \beta(Z - Z_\infty), \quad (14)$$

where a chosen macroscopic quantity  $Z$  (e.g. the pressure), and transversal waves  $\mathcal{T}_{x,i}^{\text{ex}}$ , are relaxed towards target values  $Z_\infty$  and  $\mathcal{T}_{x,i}^{\text{ex}}$  at rates  $\alpha$  and  $\beta$ , respectively. This strategy has been reported to increase numerical stability and accuracy [8]. However, the relaxation coefficients pose additional degrees of freedom that have to be determined.

Let us remark that the same strategy can be applied to the LODI approach (10), i.e.,

$$\bar{\mathcal{L}}_{x,i} = \alpha(\mathcal{T}_{x,i}^{\text{ex}} - \mathcal{T}_{x,i}) + \beta(Z - Z_\infty). \quad (15)$$

### 3.3. Realization of characteristic BC in the LBM

In the previous sections, we described how to obtain target values at the macroscopic level. We now describe how to pose these target values in a multi-speed LBM to implement a characteristic BC.

The general procedure [24, 26, 27] is summarized in Fig. 4. The starting points are the macroscopic flow fields computed by the LBM algorithm (see Sec. 2) at a generic time  $t$ . The task of the boundary condition is to define the lattice populations left undefined at the boundary of the computational domain. To this aim, we perform a spatial discretization, replacing the spatial derivatives with finite differences and enabling the computation of the discrete analog of the vector of manipulated wave amplitudes  $\bar{\mathcal{L}}_x$  given by Eq. (9). Next, we plug this vector into the corresponding macroscopic evolution and perform a time integration, delivering the macroscopic target values for the next time step  $t + \Delta t$ . Finally, the computed target values are supplied to the LBM by means of a mesoscopic Dirichlet BC, thus specifying the missing populations at time  $t + \Delta t$ .

In the remaining part of this section, we provide details on the implementation of CBC for multi-speed stencils, corner treatment and possible choices for space and time discretization.

*Multi-speed LBM.* For multi-speed LBM,  $M$  layers of boundary nodes exhibit missing populations, where  $M$  is the maximum displacement of the underlying velocity stencil. In this work, we consider the D2Q17 and D2Q37 velocity stencils (Fig. 1), both having maximum displacement  $M = 3$ . Let us label the boundary nodes at the right hand side boundary, for a fixed  $y$ , as  $\mathbf{x}_{b,j} = (x_{b,j}, y)$ ,  $j = 1, \dots, M$ , where  $\mathbf{x}_{b,1}$  is adjacent to the rightmost fluid node  $\mathbf{x}_f = (x_f, y)$  and  $\mathbf{x}_{b,M}$  is the outermost boundary node (see Fig. 5). The characteristic analysis is conducted for each layer of boundary nodes. As explained in Sec. 3.1, waves crossing the  $j$ -th layer of boundary nodes are identified by the sign of the corresponding eigenvalue and the incoming wave amplitude variations are posed on  $\mathbf{x}_{b,j}$ . Note that the resulting target values may differ for the various layers forming the boundary. Finally, the macroscopic equation describing the time evolution of  $\mathbb{U}$  on the boundary is solved numerically. Details on the numerical solution are reported in the paragraphs below.

*Spatial discretization and corner treatment.* The spatial derivatives of macroscopic quantities  $\mathbb{U}$  on a boundary node  $\mathbf{x}_{b,j}$  at a fixed time  $t$  are approximated with second order finite differences. Dropping the fixed time  $t$  for the sake of a compact notation, we denote a spatial discretization step in  $x$ -direction by  $\mathbf{e}_x = (\Delta x, 0)^\top$ . For  $\mathbf{x}_{b,M}$  (outer most layer), we use one-sided differences for the spatial derivatives:

$$\frac{\partial \mathbb{U}_i(\mathbf{x}_{b,M})}{\partial x} \approx \frac{1}{2} (3\mathbb{U}_i(\mathbf{x}_{b,M}) - 4\mathbb{U}_i(\mathbf{x}_{b,M-1}) + \mathbb{U}_i(\mathbf{x}_{b,M-2})). \quad (16)$$

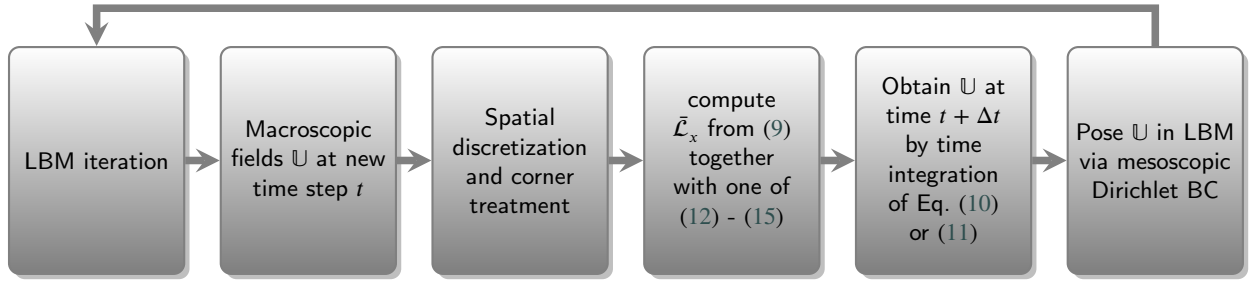


Figure 4: Flowchart of the conceptual steps required to pose a CBC in the LBM.

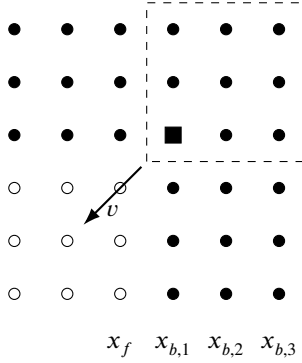


Figure 5: Schematic boundary geometry for multi-speed velocity stencils with a displacement of  $M = 3$ . Filled (hollow) symbols denote boundary (bulk) nodes. To pose a characteristic BC, finite differences are applied to approximate spatial derivatives in the boundary nodes. The square node is used to calculate the target macroscopic quantities for all corner nodes in the dashed rectangle. In this case, spatial derivatives are evaluated along the inward diagonal  $v$  indicated by the arrow.

For inner boundary nodes  $\mathbf{x}_{b,j}$ ,  $j = 1, 2, \dots, M - 1$ , we use central finite differences for the derivatives:

$$\frac{\partial U_i(\mathbf{x}_{b,j})}{\partial x} \approx \frac{1}{2} (U_i(\mathbf{x}_{b,j} + \mathbf{e}_x) - U_i(\mathbf{x}_{b,j} - \mathbf{e}_x)). \quad (17)$$

Spatial derivatives in  $y$ -direction are evaluated analogously. Corners between two open boundaries are treated using the LODI approach. That is, target macroscopic values are obtained from plugging Eq. (12) in the LODI approach (10). Spatial derivatives are computed in the direction of the inward facing diagonal, e.g. for the top right corner it is along the direction  $v = (-1, -1)^\top$ , see Fig. 5. This is only done for the innermost corner node (square node in Fig. 5) and the obtained target values are posed on all nodes forming the corner (dashed box in Fig. 5).

*Evaluation of viscous terms.* Using the CBC approach described in this work (see Tab. 1), we aim to reconstruct the Navier-Stokes-Fourier equations on the boundary. This should be contrasted with the recent implementation of characteristic BCs for multi-speed LBM given in [32], where the focus was on acoustic problems and thus the viscous terms were discarded.

Name	Macroscopic Eq.	Incoming amplitude
LODI	(10)	(12)
LODI-RELAX	(10)	(15)
CBC	(11)	(13)
CBC-RELAX	(11)	(14)

Table 1

Summary of the characteristic based BC considered in this work.

To ensure consistency in the coupling of mesoscopic and macroscopic scales at the boundary, we make use of the link between the scales provided by the Chapman-Enskog expansion. This multiscale expansion offers expressions for the viscous terms on the macroscopic scale in terms of the mesoscopic distribution.

That is, the Laplacian of velocity appearing in Eq. (7) is approximated as [33]

$$\mu \partial_{jj} u_k \approx \nabla_j \cdot \left( - \left( 1 - \frac{1}{2\tau} \right) \sum_{i=1}^q c_{i,j} c_{i,k} f_i^{\text{neq}} \right), \quad (18)$$

where the derivatives of the non-equilibrium part  $f_i^{\text{neq}} = f_i^{\text{eq}} - f_i$  are evaluated in  $\mathbf{x}_f$  – i.e. in the fluid node adjacent to the boundary (see Fig. 5) – using the finite differences (16) and (17) (along  $y$ ). Furthermore, making use of Eq. (3), the Laplacian of the temperature is restated as

$$-\kappa \partial_{jj} T = \text{div}(\mathbf{q}) = \nabla \cdot \frac{1}{2} \sum_{i=1}^q f_i |\mathbf{c}_i - \mathbf{u}|^2 (\mathbf{c}_i - \mathbf{u}). \quad (19)$$

For a sufficiently high order quadrature, which allows recovery of the third order moment of the distribution, it is then possible to compute the above quantity and to then approximate the first order spatial derivatives of  $\mathbf{q}$  using finite differences (e.g. (16) or (17)).

To conclude, in Table 1 we summarize the different CBC schemes which will be evaluated in numerical simulations in the upcoming sections.

*Time integration.* The implementation of a characteristic BC requires time integration of either Eq. (10) or Eq. (11). As pointed out in Ref. [32], a simple explicit Euler scheme is not a viable option in this case since the coupling with LBM leads to the violation of the CFL condition for the FD solver. Therefore, we make use of a fourth order Runge-Kutta

scheme (RK4) [39], which requires derivative information at time  $t + \frac{\Delta t}{2}$  approximated using the second order finite differences shown above. Macroscopic quantities located on fluid nodes at this intermediate stage are obtained by linear interpolation in time.

For the time integration of the CBC scheme, we keep the viscous terms (18) and (19) at time  $t$ , as on a boundary node, no populations at future time steps are known.

**Mesoscopic BC.** After the target values  $\mathbb{U}$  for time  $t + \Delta t$  have been obtained, they are enforced in the LBM by means of a Dirichlet BC. In this work, two simple ways to do this are considered: i) the equilibrium BC, where all populations on  $\mathbf{x}_{b,j}$  are set according to the discrete expansion of the equilibrium distribution chosen, e.g. according to Eq. (5) or Eq. (6) and ii) the constant non-equilibrium extrapolation BC (NEEP), where the non-equilibrium part of the fluid node  $\mathbf{x}_f$  adjacent to the boundary is added to the equilibrium computed on the boundary nodes. That is, populations on the boundary node  $\mathbf{x}_{b,j}$  are computed as (see Fig. 5 for notation  $\mathbf{x}_f$  and  $\mathbf{x}_{b,j}$ )

$$\begin{aligned} f(\mathbf{x}_{b,j}, t + \Delta t) \\ = f^{\text{eq}}(\mathbf{x}_{b,j}, t + \Delta t) + f^{\text{neq}}(\mathbf{x}_f, t + \Delta t), \end{aligned} \quad (20)$$

where  $j = 1, \dots, M$  and

$$f^{\text{neq}}(\mathbf{x}_f, t + \Delta t) = f(\mathbf{x}_f, t + \Delta t) - f^{\text{eq}}(\mathbf{x}_f, t + \Delta t).$$

## 4. Numerical Results

In this section, we benchmark accuracy and stability of the characteristic boundary condition described in the previous section. We consider three different numerical experiments. In Sec. 4.1, we take into consideration the one-dimensional dynamics of shock waves originated by a smoothed temperature step. In Sec. 4.2, we consider the propagation of a vortex out of the computational domain. In this benchmark, transversal information becomes relevant also at the boundary and thus, there is a significant deviation from the locally one-dimensional assumption used to calculate the outgoing wave amplitude variations in the LODI approximation. Finally, in Sec. 4.3, we inspect the interaction of an planar oblique wave with the boundary at various angles and measure the reflection. In this setup, the importance of transversal terms can be controlled by the initial angle between the wave front and the  $y$ -axis.

For all the cases above, we compare the performance of different LODI and CBC realizations against the results provided by a simple zero gradient BC (ZG), where populations at the boundary nodes  $\mathbf{x}_{b,j}$ ,  $j = 1, \dots, M$  are set with the values from the nearest fluid node  $\mathbf{x}_f$ :

$$f_i(\mathbf{x}_{b,j}, t + \Delta t) = f_i(\mathbf{x}_f, t + \Delta t), \quad i = 1, \dots, q. \quad (21)$$

The accuracy of the BCs is quantified as follows: For the first two benchmark problems, reference fields  $Z^{\text{ref}}$  are obtained from a fully periodic LBM simulation on an extended grid

for  $Z \in \{\rho, u_x, T\}$ . The extended grid has been chosen sufficiently large, such that no interaction takes place between the boundaries and the bulk dynamics in the region of interest. We then compute i) global relative  $L^2$ -errors  $e_Z$  and ii) pointwise relative errors  $\tilde{e}_Z$  with respect to the reference fields. They are defined as

$$\begin{aligned} e_Z &= \left( \sum_{(x,y) \in L_x \times L_y} \left( \frac{|Z(x,y) - Z^{\text{ref}}(x,y)|}{|Z^{\text{ref}}(x,y)|} \right)^2 \right)^{\frac{1}{2}}, \\ \tilde{e}_Z(x,y) &= \frac{|Z(x,y) - Z^{\text{ref}}(x,y)|}{|Z^{\text{ref}}(x,y)|}. \end{aligned}$$

### 4.1. 1D temperature step

We consider a 2D bounded rectangular domain with an initial homogeneous density  $\rho_0$ , a homogeneous background velocity  $\mathbf{u}_0$  (parallel to the  $x$ -axis) and a smooth temperature step (parallel to the  $x$ -axis, for temperature  $T_0$  to  $T_1$  and back to  $T_0$ ). Formally:

$$\begin{aligned} \rho(x,y) &= \rho_0, \quad \mathbf{u}(x,y) = \mathbf{u}_0, \\ T(x,y) &= T_1 + \frac{T_1 - T_0}{2} (\tanh(s \cdot (x - \frac{L_x}{2})) - 1). \end{aligned}$$

The initial conditions and the corresponding dynamic is sketched in Fig. 6. The specific numerical values are found in the caption of Fig. 6.

The left- and right-hand side boundaries of the rectangular domain are equipped with artificial BC. The upper and lower boundaries are taken to be periodic. For this flow, the LODI approximation underlying the computation of the wave amplitude variations is well justified: the flow is globally one dimensional and only viscous terms are discarded in the approximation.

Numerical simulations have been conducted using the D2Q17 stencil on a grid of size  $L_x \times L_y = 200 \times 20$  and the relaxation time used in simulation was  $\tau = 0.9$  in numerical units. Fig. 6 depicts the reference simulation (for  $T^{\text{ref}}$  and  $u_x^{\text{ref}}$ ) in the region of interest at selected times (from  $t_0$  initial value till  $t_3$ , where the system almost reaches a resting state).

In Fig. 7, we present the time evolution of the global relative  $L^2$ -errors  $e_Z$ . Evidently, any characteristic BC reduces the value of  $e_Z$  for all macroscopic quantities taken into consideration by two or more orders of magnitude on average. Since transversal terms are negligible for this benchmark, the only difference between the LODI and CBC implementations is the incorporation of viscous terms. It is observed that the CBC scheme leads to slightly larger errors for the first 400 iterations (i.e., before significant interaction with the boundary sets in), see Fig. 7. As explained in Sec. 3.3, this difference comes from the fact that in the RK4-scheme used for time integration of Eq. (11), no value for the heat-flux is available at the intermediate time  $t + \frac{\Delta t}{2}$  and the old value from time  $t$  is used instead. As the impinging wave starts interacting with the boundary, the error levels obtained with the CBC coincide with those of the LODI schemes in  $e_\rho$  and  $e_T$  and improve in  $e_{u_x}$ .

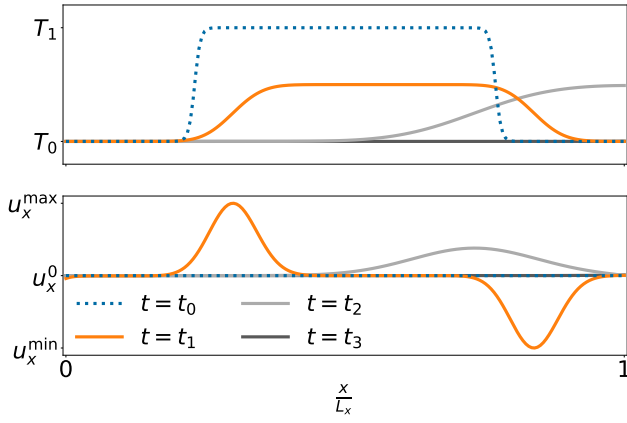


**Figure 6:** Temperature and stream-wise velocity profiles of the reference simulation at selected time steps, plotted along the horizontal centerline  $y = \frac{L_x}{2}$ . The initial configuration at  $t = t_0$  is obtained with the following parameters:  $\rho_0 = T_0 = 1, T_1 = 1.0005, \mathbf{u}_0 = (\text{Ma} \cdot c_s, 0)^\top, s = 0.5$ . The times  $t_1$  and  $t_2$  correspond to iterations shortly before and during the pulses interaction with the artificial boundary posed at  $x = L_x$  in the simulation on the truncated grid. At  $t = t_3$ , the system is almost completely at rest (see also Fig. 7 for the localization of the time instances  $t_i$ ).

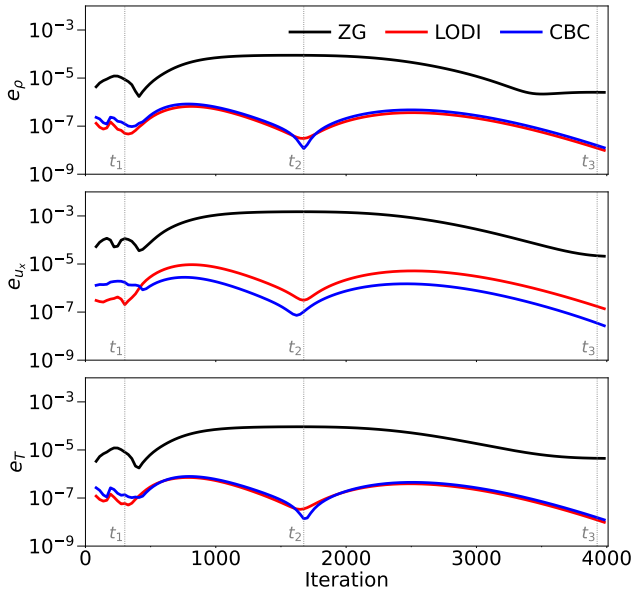


**Figure 7:** Evolution of  $e_Z$  in the thermal step benchmark with  $\tau = 0.9$ . The vertical dotted lines correspond to the times  $t_1, t_2$  and  $t_3$  in Fig. 6.

In Fig. 8, the pointwise relative errors  $\tilde{e}_Z$  along the horizontal midplane  $y = \frac{L_y}{2}$  are shown at time  $t_2$ . Consistent to the global  $L^2$ -errors, the ZG produces pointwise errors almost three orders of magnitude higher in all the points considered when compared to the characteristic schemes. In particular, the usage of the ZG scheme has a larger impact on the bulk dynamics than any characteristic based BC; we note that also the accuracy in the center of the computational

domain, away from inlet and outlet, is degraded. The LODI and CBC schemes yield very similar pointwise errors that are maximized close to the outlet, where small oscillations are introduced.

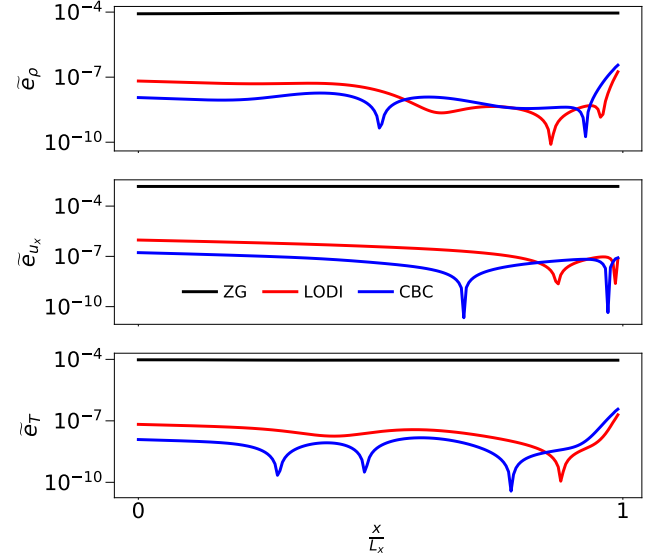


**Figure 8:** Pointwise relative errors  $\tilde{e}_Z$  at time  $t_2$  along the slice  $y = \frac{L_y}{2}$ .

## 4.2. Propagating Vortex

We consider the propagation of a thermal vortex in a rectangular computational domain of size  $L_x \times L_y = 150 \times 150$ . The initialization of the problem is described in normalized spatial coordinates  $(\hat{x}, \hat{y}) \in [-1, 1]^2$ :

$$\hat{x} = \frac{2(x-1)}{L_x-1} - 1, \quad \hat{y} = \frac{2(y-1)}{L_y-1} - 1.$$

The initial center of the vortex is defined by:

$$(\hat{x}_0, \hat{y}_0) = \left( \frac{K}{L_x-1}, 0 \right),$$

where the parameter  $K$  defines  $x$ -position of the vortex on the horizontal center line. The thermal vortex is formed by a perturbation of the temperature  $T$  around  $T_0$  within a circle at  $(\hat{x}_0, 0)$  with radius  $\hat{r}$  against a uniform background flow. We use the following initial macroscopic fields:

$$\rho(x, y) = \rho_0,$$

$$\mathbf{u}(x, y) = \mathbf{u}_0 + \begin{cases} 0 & \text{if } (\hat{x} - \hat{x}_0)^2 + \hat{y}^2 \geq \hat{r}^2 \\ \mathbf{v}(\hat{x} - \hat{x}_0, \hat{y}) & \text{otherwise,} \end{cases}$$

$$T(x, y) = T_0 + \begin{cases} 0 & \text{if } (\hat{x} - \hat{x}_0)^2 + \hat{y}^2 \geq \hat{r}^2 \\ \theta(\hat{x} - \hat{x}_0, \hat{y}) & \text{otherwise,} \end{cases}$$

the vortex strength in terms of the initial perturbations is given in terms of a parameter  $b$  as

$$\mathbf{v}(x, y) = \frac{5c_s \text{Ma}}{2} 2^{-\frac{x^2+y^2}{b^2}} \begin{pmatrix} y \\ -x \end{pmatrix},$$

$$\theta(x, y) = \frac{5c_s \text{Ma}}{2} 2^{-\frac{x^2+y^2}{b^2}}. \quad (22)$$

The setup is illustrated in Fig. 9. The Eckert number corresponding to the simulation parameters is  $\text{Ec} \approx 0.02$ .

For the evaluation of the ZG BC, all boundary nodes are subjected to Eq. (21). The various characteristic based BCs summarized in Table 1 are applied at the right hand side boundary, while the LODI scheme is used for the other straight boundaries. Corner nodes are treated as discussed in Sec. 3.3.

Contrary to the previous benchmark, this test exhibits fully two-dimensional dynamics. Therefore, it is more challenging with respect to the BC.

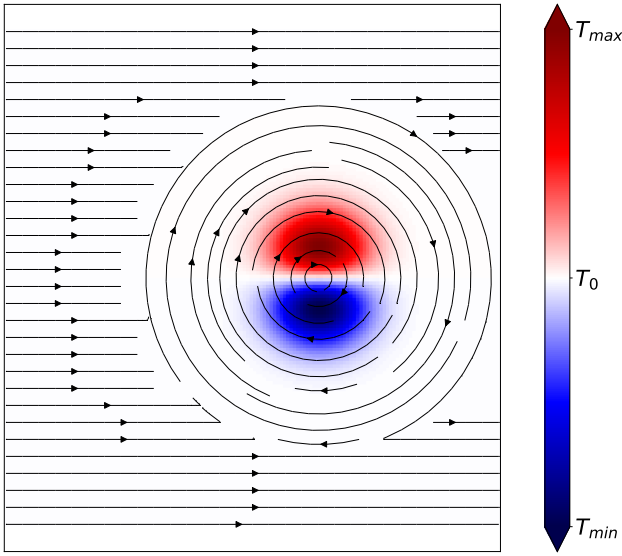


**Figure 9:** Initial setup for thermal vortex benchmark in the computational domain. Temperature  $T(x, y)$  (heat map) varies around  $T_0 = 1$  in a circle with center  $(\hat{x}_0, \hat{y}_0)$  with radius  $\hat{r} = 0.7$  and strength  $b = \frac{3}{20}$ , see (22). The initial velocity field (streamlines) is the superposition with a global background velocity  $\mathbf{u}_0 = (\text{Ma} \cdot c_s, 0)^\top$  and the vortex. Here, we use  $\text{Ma} = 0.1$ .

At the outlet (right-hand side boundary), we need to specify the wave amplitude  $\bar{\mathcal{L}}_{x,3}$  (see Fig. 3). The schemes with relaxation given by Eqns. (14) and (15) require the definition of the two relaxation parameters  $\alpha$  and  $\beta$ . Following Ref. [8], we set  $\alpha = \text{Ma}$ ,  $\beta = 0$ , and  $\mathcal{T}_{x,3}^{\text{ex}} = 0$ . This choice of parameters implies that transversal waves vanish at the steady state.

We start by considering a numerical viscosity of  $\nu = 0.1$ , corresponding to Knudsen number  $\text{Kn} = \frac{\nu}{c_s L_x} \approx 0.0011$ .

The corresponding evolution of  $e_Z$  for the various BC is shown in Fig. 10. It can be seen that in comparison with the LODI scheme, incorporating a relaxation of the transversal wave in the incoming wave amplitude reduces global errors by about one order of magnitude in the time range going between 400 to 1000 iterations. Their similar error levels indicate that at least for this benchmark, encoding external information in the incoming wave amplitude is much more

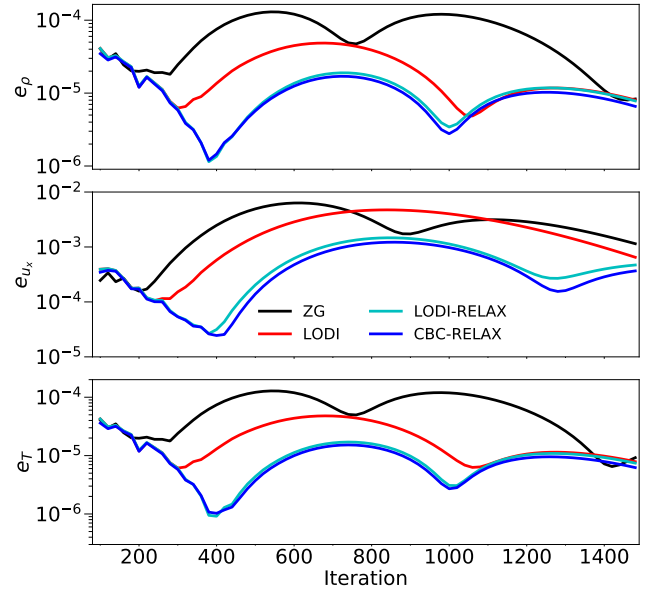


**Figure 10:** Evolution of relative  $L^2$ -errors in macroscopic fields at  $\nu = 0.1$ .

important than accounting for transversal information in the macroscopic system at the boundary. We remark that, in general, it is not known how to choose the optimal values for the relaxation parameters. For this specific benchmark, we have performed a parameter scan in  $\alpha$  for values around  $\alpha = \text{Ma}$  and found that the average values of  $e_Z$  can be reduced by about 33 percent for  $\alpha = \frac{2}{3}\text{Ma}$ .

The ZG BC gives similar results as the characteristic based BCs in the first 200 iterations. Apart from the iterations between 700 and 1100, where the value of  $e_{u_x}$  is smaller than its LODI-counterpart, it gives the largest global errors among all the BC considered. In Figs. 11 and 12, we provide snapshots of pointwise relative errors (with respect to the reference solution) for the downstream velocity and temperature at selected time steps. For all the BC, small scale errors in both temperature and downstream velocity are observed at the boundaries after 100 iterations (first selected time step), as an initial spherical pressure pulse interacts with the boundaries. The vortex interaction with the boundary soon becomes the dominant source of error. As can be seen from the right-most columns in both figures, the vortex reaches the boundary after about 400 iterations. From this point onwards, the relaxation approach gives a significant advantage over both the LODI and ZG BC. During the vortex-boundary interaction, here exemplified at 800 and 1200-iterations, the ZG is systematically outperformed. We observe that characteristic based schemes allow to better capture the interaction with the boundary, and moreover the bulk region is significantly less polluted. In this benchmark, we have used the CBC-RELAX scheme in combination with the equilibrium BC (5) which under these settings provide similar results to the NEEP BC (20).

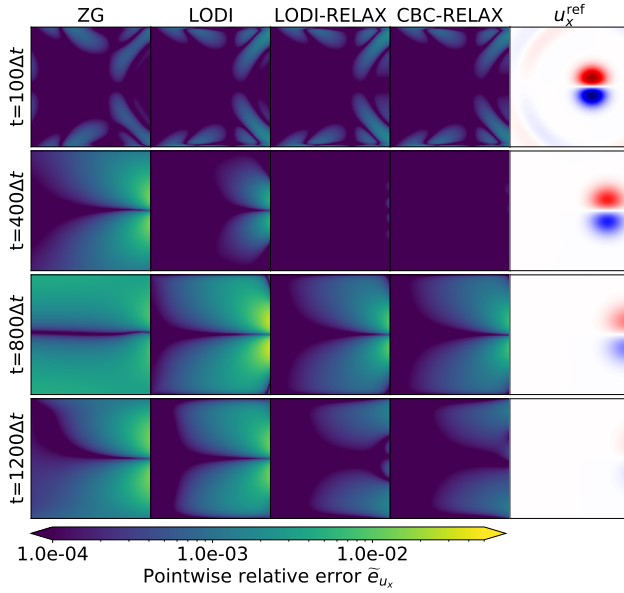


**Figure 11:** Heat maps of relative errors for the downstream velocity for various versions of the BC conditions (vortex example). The right column give our reference solution. In the rows, we have snapshots at  $t = 100\Delta t$  (initial phase),  $t = 400\Delta t$  (the vortex has reached about the boundary),  $t = 800\Delta t$  (center of the vortex is on the boundary),  $t = 1200\Delta t$  (late phase, where the vortex has almost left the domain of interest).

*Treatment of viscous terms.* We found the evaluation of viscous terms from Eqns (18) and (19) crucial to ensure numerical stability over a broad range of numerical viscosity  $\nu$ . To illustrate this, simulations at various values of  $\nu$  have been conducted comparing with a CBC formulation where the Laplacian of temperature and velocity are approximated using second order finite differences. In particular, we use the backward formula for  $j = M$

$$\frac{\partial^2 \mathbb{U}_i(\mathbf{x}_{b,M}, t)}{\partial^2 x} \approx 2\mathbb{U}_i(\mathbf{x}_{b,M}, t) - 5\mathbb{U}_i(\mathbf{x}_{b,M} - \mathbf{e}_x, t) + 4\mathbb{U}_i(\mathbf{x}_{b,M} - 2\mathbf{e}_x, t) - \mathbb{U}_i(\mathbf{x}_{b,M} - 3\mathbf{e}_x, t)$$

and central formula for  $j = 1, 2, \dots, M - 1$

$$\frac{\partial^2 \mathbb{U}_i(\mathbf{x}_{b,j}, t)}{\partial^2 x} \approx \mathbb{U}_i(\mathbf{x}_{b,j} + \mathbf{e}_x, t) - 2\mathbb{U}_i(\mathbf{x}_{b,j}, t) + \mathbb{U}_i(\mathbf{x}_{b,j} - \mathbf{e}_x, t).$$

The resulting scheme is referred to with the suffix -FD. Note that this scheme can be used when working with stencils which do not allow to implement high order quadrature.

In the first two rows of Fig. 13, we show the heat maps of  $\tilde{e}_T$  after 1200 iterations for several different values of the kinematic viscosity. For  $\nu = 0.1$ , we observe that the two methods yield very similar temperature fields. In the last row of this figure, we report the time evolution of the Laplacian of  $T$  evaluated at point  $P = (x_0, y_0)$  in proximity of the outlet (cf. top left panel in Fig. 13). The mesoscopic evaluation of this quantity is closely following the evolution of ground

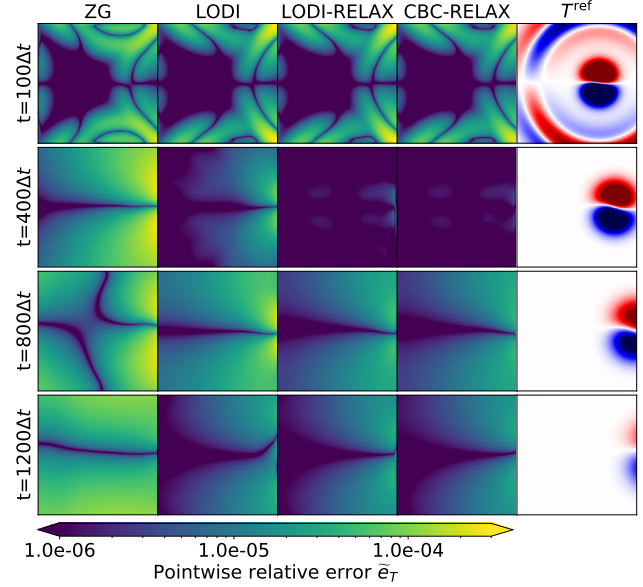


**Figure 12:** Heat maps of relative errors in temperature and reference solution on the right column (vortex example). In the rows, we have snapshots at  $t = 100\Delta t$  (initial phase),  $t = 400\Delta t$  (the vortex has reached about the boundary),  $t = 800\Delta t$  (center of the vortex is on the boundary),  $t = 1200\Delta t$  (late phase, where the vortex has almost left the domain of interest).

truth, whereas its finite difference counterpart exhibit larger and larger discrepancies, which become more evident as the viscosity is increased, eventually leading to numerical instabilities at  $\nu = 0.3$ .

*Effect of the underlying velocity stencil.* The characteristic BC developed in this work can be applied to any LBM stencil, provided that the macroscopic target values returned by the artificial boundary are supplied at the mesoscopic layer with a suitable Dirichlet BC. As an example, in this section, we compare the results from simulations employing the D2Q37 velocity stencil. In Table 2, we report the arithmetic means, maximum value (over time) and the empirical standard deviation  $s$  of error quantity  $e_Z$  ( $Z \in \{\rho, u_x, T\}$ ). For a simple read out, errors are normalized with respect to the D2Q17 simulation using the ZG BC.

The overall behavior of errors is similar for both stencils. Switching from a ZG BC to LODI, the global errors in  $\rho$  and  $T$  decrease by roughly a factor of two, while the velocity fields are not significantly improved. However, tuning the relaxation parameters in the inward pointing wave amplitude allows to further decrease the errors in the velocity field. Switching the macroscopic equation that is solved on the boundary give further small improvements in accuracy. The errors for  $\rho$  and  $T$  are approximately same for the two different stencils.

### 4.3. Angular Wave

In this section, we consider an impinging plane wave that approaches the boundary at an angle  $\phi$  with respect to the vertical line ( $x = x_b$ , left boundary); i.e.,  $\phi = 0$  states

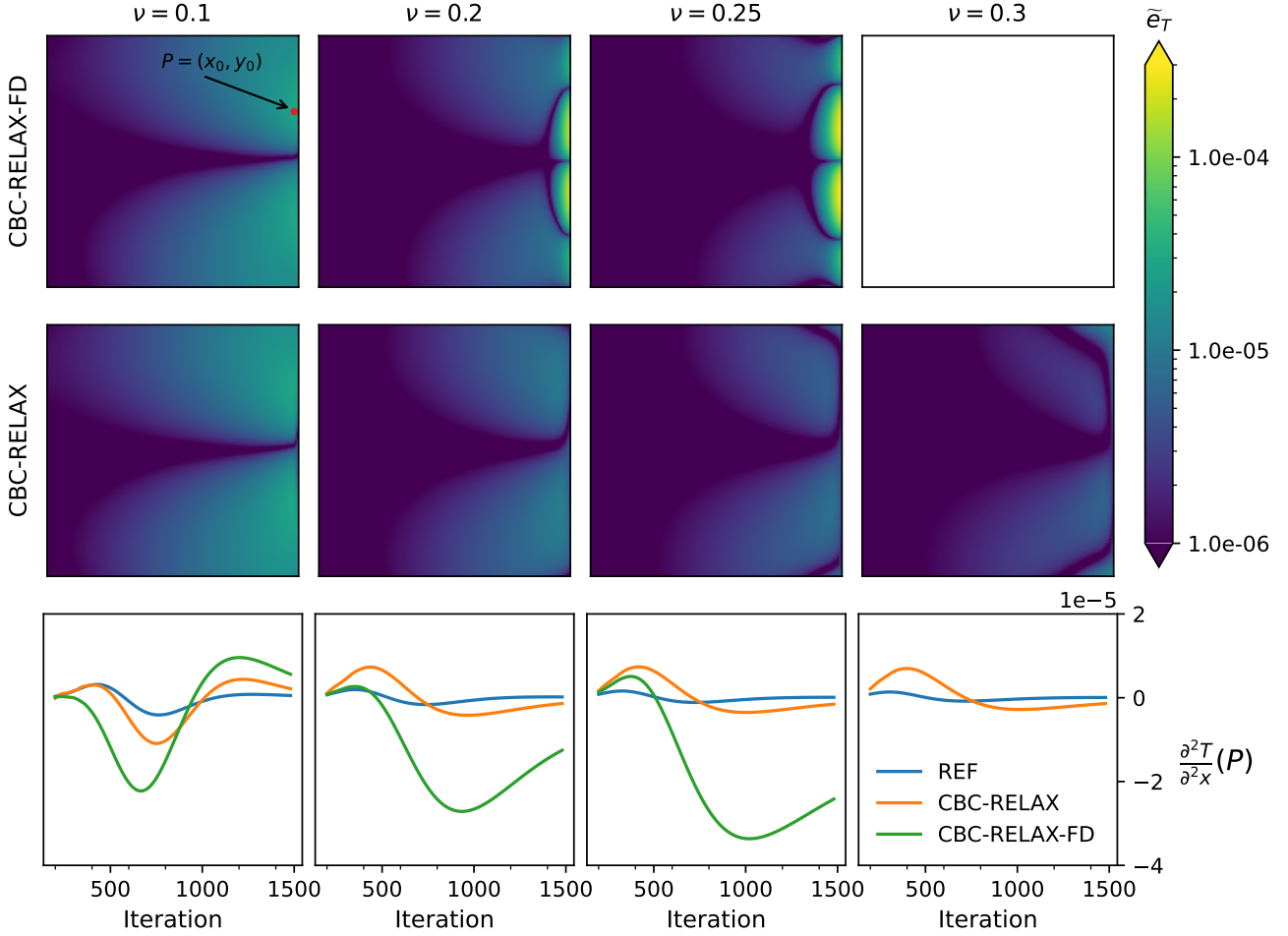


**Figure 13:** Upper and middle panels show heat maps of the relative errors in temperature  $T$  after 1200 iterations at various numerical viscosity ranging from  $\nu = 0.1$  (first column) to  $\nu = 0.3$  (right column). The lower panel shows the time evolution of the quantity  $\frac{\partial^2 T}{\partial x^2}$  computed at  $P = (x_0, y_0)$  marked in red in the top left panel. It can be seen that increasing the numerical viscosity, the coupling between the macroscopic solver on the boundary and the LBM gives rise to an instability when the Laplacian is evaluated directly at the macroscopic level rather than at the mesoscopic one.

that the plane wave propagates in the direction normal to the boundary. In this setup, as the value of  $\phi$  is increased, the transversal contributions become more and more important, in turn departing from the LODI approximation.

We evaluate the BCs ability to absorb outgoing information by computing a reflection coefficient. To this end, we calculate wave amplitudes before and after the interaction with the boundary takes place (from simulation data) and compute their ratio along the horizontal midplane.

The initial setup at time  $t_0$  reads

$$\begin{aligned} \rho(x, y) &= \rho_0, \quad \mathbf{u}(x, y) = \mathbf{u}_0, \\ T(x, y) &= T_0 + \frac{1}{10} \exp\left(\frac{-\hat{x}(x, y)^2}{2s^2}\right), \end{aligned}$$

where the shifted coordinates

$$\hat{x}(x, y) = \begin{pmatrix} \cos(\phi \frac{\pi}{180}) \\ \sin(\phi \frac{\pi}{180}) \end{pmatrix} \cdot \begin{pmatrix} x \\ y \end{pmatrix}$$

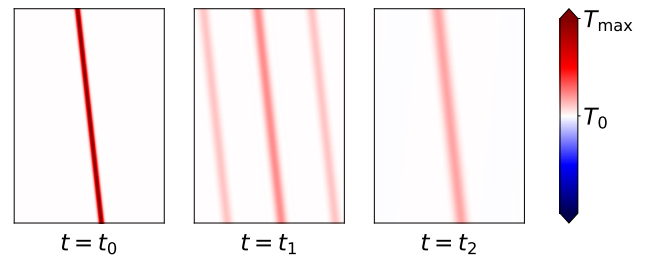


**Figure 14:** Temperature fields obtained using the LODI BC at various time steps. The left panel depicts the initial state at time  $t_0$  with initial conditions given by  $\rho_0 = T_0 = 1$ ,  $\mathbf{u}_0 = (0, 0)^T$  and  $s = \frac{1}{50}$ . The times  $t_1$  and  $t_2$  correspond to before and after waves interacted with the left hand side boundary at height  $y = \frac{L_y}{2}$  respectively.

are used. The upper and lower boundaries are periodic, while artificial boundaries are set at the left and right hand side of the domain. We chose a numerical viscosity of  $\nu = 0.1$  and

	ZG		LODI		LODI-RELAX		CBC-RELAX	
	avg $\pm$ SEM	max	avg	max	avg	max	avg	max
$e_{\rho}^{17}$	$6.4 \cdot 10^{-5} \pm 4.8 \cdot 10^{-6}$	$1.3 \cdot 10^{-4}$	0.32	0.37	0.18	0.32	0.16	0.27
$e_{\rho}^{37}$	$7.5 \cdot 10^{-5} \pm 7.0 \cdot 10^{-6}$	$1.6 \cdot 10^{-4}$	0.33	0.36	0.18	0.35	0.18	0.32
$e_{u_x}^{17}$	$2.5 \cdot 10^{-3} \pm 2.1 \cdot 10^{-4}$	$6.3 \cdot 10^{-3}$	0.82	0.75	0.22	0.23	0.18	0.19
$e_{u_x}^{37}$	$3.0 \cdot 10^{-3} \pm 3.0 \cdot 10^{-4}$	$7.4 \cdot 10^{-3}$	0.78	0.77	0.22	0.22	0.18	0.18
$e_T^{17}$	$6.3 \cdot 10^{-5} \pm 4.8 \cdot 10^{-6}$	$1.3 \cdot 10^{-4}$	0.32	0.37	0.17	0.33	0.15	0.28
$e_T^{37}$	$7.4 \cdot 10^{-5} \pm 6.9 \cdot 10^{-6}$	$1.6 \cdot 10^{-4}$	0.34	0.37	0.18	0.36	0.17	0.32

**Table 2**

Comparison of the obtained accuracy the vortex benchmark using D2Q17 and D2Q37 velocity stencils: We compare arithmetic mean of the sampled global errors  $e_Z$ , the corresponding standard error of the mean (SEM) and their maximum value (over time). Results are normalized with respect to the values obtained for the ZG BC and the respective stencil (left table). The SEM has been omitted from the right hand side table as it scales similarly to the average error.

conducted simulations on a  $L_x \times L_y = 200 \times 700$  grid. The domain is chosen to be sufficiently large to ensure that the measurements at the horizontal centerline are not polluted by artifacts stemming from the periodicity of the upper and lower boundaries. We perform simulations at various angles  $\phi$ , tracking wave amplitudes for the macroscopic quantities  $Z \in \{\rho, u_x, T\}$  along the horizontal slice  $y = \frac{L_y}{2}$ . The measurements are taken at a time  $t_1$  and  $t_2$ , respectively shortly before and right after the interaction with the boundaries (cf. Fig. 14). The reflection coefficient is then computed as

$$R_Z = \frac{I_Z(t_2)}{I_Z(t_1)}.$$

Snapshots of the temperature profiles at times  $t_0, t_1, t_2$  are shown in Fig. 14 showing the initial state and the state before and after the boundary interaction of the angular wave. In Fig. 15, we report the reflection coefficient  $R_{\rho}$  over

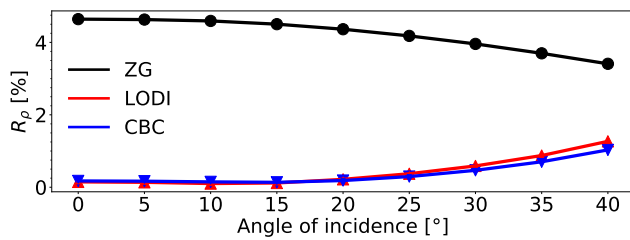


**Figure 15:** Angular dependency of the reflection coefficient  $R_{\rho}$  along the horizontal slice  $y = \frac{L_y}{2}$ , on a  $L_x \times L_y = 200 \times 700$  grid.

a range of values for the angle  $\phi$ . The reflection coefficients for temperature and streamwise velocity gives very similar results and are hence omitted here. We observe that the ZG BC gives rise to reflected waves with about four percent of the impinging waves amplitude. For small angles  $\phi < 15^\circ$ , the usage of the (perfectly non-reflecting) CBC reduces reflections by roughly one order of magnitude. As  $\phi$  is increased further, we observe a growth in reflections caused by the characteristic based schemes. This can be attributed to two factors. First, as already mentioned, for non-zero

values of  $\phi$  the dynamic starts departing from the LODI approximation. Second, waves impinging at large values of  $\phi$  interact with the boundary for longer time with respect to waves at smaller angles, putting further stress on the BC. Nevertheless, the advantage of CBC over the ZG BC is still retained at a  $40^\circ$  angle, where reflection coefficient is reduced by a factor of about three.

As already discussed in Sec. 4.1, the reincorporation of transversal terms in the CBC scheme gives rise to small oscillations close to the outlet. This leads to slightly higher reflection coefficients at angles  $\phi < 25^\circ$  when compared to the LODI scheme. However, at angles  $\phi > 25^\circ$ , the error in discarding transversal information becomes dominant and the LODI scheme gives rise to larger reflection coefficients than the CBC.

#### 4.4. Corners and multi-speed models

In previous sections, we have discussed implementation and numerical results for characteristic based BC applied to multi-speed thermal LBM. These models require the application of BC to several layers of nodes, which can lead to small oscillations at the interface between the boundary and the bulk domain (see again Fig. 8), although such spurious effects can be mitigated resorting to a mesoscopic evaluation of the partial derivatives for velocity and temperature field (Fig. 13). The complexities associated to handling multiple boundary layers are emphasized when dealing with corner nodes (see Fig. 5). While there exist compatibility conditions [10] to be posed at overlapping boundaries, their application to corners formed by several nodes in a multi-speed setting is not immediately obvious. For this reason, we have relied on a simple LODI approximation for the treatment of corners of the computational domain. In order to assess the impact of corners in simulation results, in this section, we consider simulations for the propagation of a iso-thermal vortex. The numerical setup is exactly the same as for the thermal flow discussed in Sec. 4.2 with the only difference that we start now from a uniform temperature profile, whose time evolution is suppressed. This allows to compare the results of simulations from multi-speed models with those given

by the single-speed D2Q9 model. Details on all the stencils used are given in Appendix B. In Fig. 16, we show heat maps for both quantities  $\tilde{e}_\rho$  and  $\tilde{e}_{u_x}$ . As was done in Sec. 4.2, the CBC-RELAX scheme, with  $\alpha = \text{Ma}$ ,  $\beta = 0$ , and  $\mathcal{T}_{x,3}^{\text{ex}} = 0$  was used. In order to allow for a direct comparison between the different numerical scheme, we show results at the re-scaled time  $t^* = \lfloor 150c_s^{17}/c_s^q \rfloor$   $q \in \{9, 17, 37\}$ , where  $c_s^q$  is the speed of sound in the lattice for the different stencils (see Appendix B). Such a value is chosen in order to analyze a time frame where reflections caused at the outlet and lateral boundaries are interacting with each other close to the corners of the computational domain, which is putting under stress the corner boundary. From the results, we can observe that the dynamic obtained with the D2Q9 stencil is qualitatively and quantitatively matching that provided by multi-speed stencils. Therefore, we can conclude that the potentially extra source of inaccuracy given by the corner treatment in multi-speed stencils is negligible, at least for the benchmark here considered.

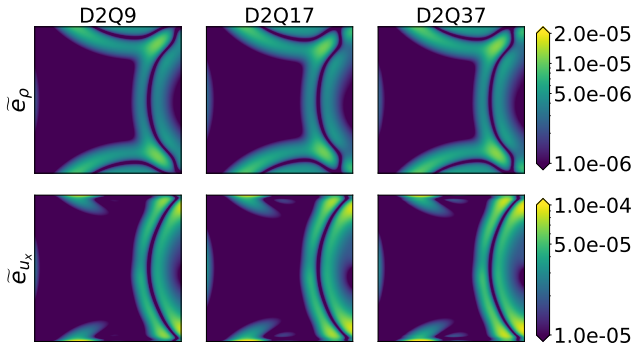


**Figure 16:** Comparison of pointwise relative errors obtained in the simulation of an iso-thermal vortex using the D2Q9, D2Q17 and D2Q37 velocity stencil.

## 5. Conclusion

In this work, we have presented a non-reflecting BC for thermal LBM, applying the concept of characteristic boundary conditions to flows governed by the Navier-Stokes-Fourier system. The procedure allows to compute outgoing wave amplitude variations from a hyperbolic system using the LODI approximation, and aims at modulating the amplitude of incoming waves in order to minimize their impact on the bulk dynamics. By constraining the amplitude of incoming waves (annihilation, relaxation towards target values), it is possible to compute the macroscopic fields at the boundary layer, which are then translated at the mesoscopic level into lattice populations.

While the procedure is general and can be applied to any of the different possible approaches for the simulation of thermal flows in LBM, we have focused our analysis on high order models based on multi-speed stencils. We have shown that this approach offers the advantage that the evaluation of the Laplacian for temperature and velocity can be established exploiting the exact calculation of the higher

	Temperature step: CBC		Vortex: CBC-RELAX	
	avg	max	avg	max
$e_\rho$	0.007	0.009	0.16	0.27
$e_{u_x}$	0.001	0.002	0.18	0.19
$e_T$	0.006	0.009	0.15	0.28

**Table 3**

Summary of the gains in accuracy normalize with respect to the global relative errors  $e_z$  obtained using the D2Q17 stencil and the ZG BC. Shown are the arithmetic mean of the sampled global errors  $e_z$  and their maximum value (over time). The SEM has been omitted as it scales very similar to the average error.

order moments of the particle distribution function, hence on the same mesoscopic footstep as LBM, in turn avoiding the need of finite difference approximations. Our numerical results highlight that this approach leads to more accurate results as well as enhanced stability at increasingly large values of the kinematic viscosity. Moreover, we have compared several CBC schemes against a zero-gradient BC, a commonly adopted strategy for the implementation of artificial boundary in literature. Table 3 provides a summary of our findings, showing that for flows with a strongly  $1 - d$  propagation direction, i.e., where the LODI approximation fully applies, the CBC outperforms the ZG BC by 2 to 3 order of magnitudes. This gap is reduced to about one order of magnitude when investigating flows with a significant transversal component. In the second case, further improvement can be obtained by relaxing the macroscopic fields to desired target values, although this generally requires tuning of extra parameters, for which the optimal value is not known a priori.

In future works, we plan to evaluate CBC, possibly in combination with the perfectly matched layer approach, in more involved kinematic regimes e.g. at large values for the Reynolds and Rayleigh number. Investigating proper compatibility conditions for the corner and flux-splitting methods appear to be further important and promising directions for future research.

## Appendix

### A. CBC and LODI for Navier-Stokes-Fourier in $d = 3$ spatial dimensions

In this appending section, we provide the ingredients necessary to extend the implementation of the characteristic based BC for the Navier-Stokes-Fourier in  $d = 3$  spatial dimensions. We follow the same procedure discussed in the main text, and consider as an example the case of a right hand side boundary. Here, the macroscopic velocity is given as  $\mathbf{u} = (u_x, u_y, u_z)^\top$  and the transversal directions are  $\mathbf{u}_t = (u_y, u_z)^\top$  (for a boundary  $x = x_b$  constant). Furthermore, we denote the spatial gradient in the transversal directions as  $\nabla_t = (\frac{\partial}{\partial y}, \frac{\partial}{\partial z})^\top$ .

The specific heat quantities read

$$c_v = \frac{d}{2} = \frac{3}{2}, c_p = \frac{d}{2} + 1 = \frac{5}{2}$$

with ratio  $\gamma = \frac{c_p}{c_v} = \frac{5}{3}$ .

Following the same matrix representation from (8), we have here

$$A = \begin{pmatrix} u_x & \rho & 0 & 0 & 0 \\ \tilde{T} & u_x & 0 & 0 & c_s^2 \\ \rho & 0 & u_x & 0 & 0 \\ 0 & 0 & 0 & u_x & 0 \\ 0 & \frac{\tilde{T}}{c_s^2 c_v} & 0 & 0 & u_x \end{pmatrix},$$

$$\mathbb{T} = \begin{pmatrix} -\frac{\partial(\rho u_y)}{\partial y} - \frac{\partial(\rho u_z)}{\partial z} \\ -\mathbf{u}_t \cdot (\nabla_t \mathbf{u}_x) \\ -\frac{1}{\rho} \frac{\partial(\rho \tilde{T})}{\partial y} - \mathbf{u}_t \cdot (\nabla_t u_y) \\ -\frac{1}{\rho} \frac{\partial(\rho \tilde{T})}{\partial z} - \mathbf{u}_t \cdot (\nabla_t u_z) \\ -\frac{\tilde{T}}{c_s^2 c_v} \nabla_t \cdot \mathbf{u}_t - \frac{1}{c_s^2} \mathbf{u}_t \cdot \nabla_t \tilde{T} \end{pmatrix}$$

and

$$\mathbb{V} = \begin{pmatrix} 0 \\ v \left( \Delta u_x + \frac{1}{3} \frac{\partial}{\partial x} \operatorname{div} \mathbf{u} \right) \\ v \left( \Delta u_y + \frac{1}{3} \frac{\partial}{\partial y} \operatorname{div} \mathbf{u} \right) \\ v \left( \Delta u_z + \frac{1}{3} \frac{\partial}{\partial z} \operatorname{div} \mathbf{u} \right) \\ \frac{v\gamma}{\operatorname{Pr} c_s^2} \Delta \tilde{T} + \frac{v}{c_v c_s^2} \left( V_1 + \frac{2}{3} V_2 \right) \end{pmatrix},$$

where

$$V_1 = \left( \frac{\partial u_x}{\partial y} + \frac{\partial u_y}{\partial x} \right)^2 + \left( \frac{\partial u_x}{\partial z} + \frac{\partial u_z}{\partial x} \right)^2 + \left( \frac{\partial u_y}{\partial z} + \frac{\partial u_z}{\partial y} \right)^2$$

$$V_2 = \left( \frac{\partial u_x}{\partial x} - \frac{\partial u_y}{\partial y} \right)^2 + \left( \frac{\partial u_x}{\partial x} - \frac{\partial u_z}{\partial z} \right)^2 + \left( \frac{\partial u_y}{\partial y} - \frac{\partial u_z}{\partial z} \right)^2.$$

The diagonalization of  $A$  gives  $A = S^{-1} \Lambda S$  with

$$\Lambda = \operatorname{diag} \left( u_x, u_x, u_x, u_x - \sqrt{\gamma \tilde{T}}, u_x + \sqrt{\gamma \tilde{T}} \right),$$

$$S = \begin{pmatrix} -\frac{2\tilde{T}}{5\rho c_s^2} & 0 & 0 & 0 & \frac{3}{5} \\ 0 & 0 & 0 & 1 & 0 \\ 0 & 0 & 1 & 0 & 0 \\ \frac{\tilde{T}}{5\rho c_s^2} & -\sqrt{\frac{\tilde{T}}{15c_s^4}} & 0 & 0 & \frac{1}{5} \\ \frac{\tilde{T}}{5\rho c_s^2} & \sqrt{\frac{\tilde{T}}{15c_s^4}} & 0 & 0 & \frac{1}{5} \end{pmatrix},$$

$$S^{-1} = \begin{pmatrix} -\frac{\rho c_s^2}{\tilde{T}} & 0 & 0 & \frac{3\rho c_s^2}{2\tilde{T}} & \frac{3\rho c_s^2}{2\tilde{T}} \\ 0 & 0 & 0 & -\sqrt{\frac{15c_s^4}{4\tilde{T}}} & \sqrt{\frac{15c_s^4}{4\tilde{T}}} \\ 0 & 0 & 1 & 0 & 0 \\ 0 & 1 & 0 & 0 & 0 \\ 1 & 0 & 0 & 1 & 1 \end{pmatrix}.$$

indices $i$	velocities $c_i$	weights $\omega_i$
1	(0, 0)	$\frac{4}{9}$
2 – 5	(1, 0)	$\frac{1}{9}$
6 – 9	(1, 1)	$\frac{1}{36}$

**Table 4**

Discrete velocity set for the D2Q9 stencil. The stencil speed of sound is  $c_s = \frac{1}{\sqrt{3}}$ .

indices $i$	velocities $c_i$	weights $\omega_i$
1	(0, 0)	0.40200514690911
2 – 5	(1, 0)	0.11615486649778
6 – 9	(1, 1)	0.03300635362298
10 – 13	(2, 2)	0.00007907860216
14 – 17	(3, 0)	0.00025841454978

**Table 5**

Discrete velocity set for the D2Q17 stencil. The stencil speed of sound is  $c_s \approx 0.60848325122252$ .

indices $i$	velocities $c_i$	weights $\omega_i$
1	(0, 0)	0.23315066913235
2 – 5	(1, 0)	0.10730609154221
6 – 9	(1, 1)	0.05766785988879
10 – 13	(2, 0)	0.01420821615845
14 – 21	(2, 1)	0.00535304900051
22 – 25	(2, 2)	0.00101193759267
26 – 29	(3, 0)	0.00024530102775
30 – 37	(3, 1)	0.00028341425299

**Table 6**

Discrete velocity set for the D2Q37 stencil. The stencil speed of sound is  $c_s \approx 0.83543600713620$ .

The macroscopic fields at the boundary can be then calculated using the CBC approach by solving Eq. (11), or Eq. (10) for LODI.

## B. Data on velocity stencils

In this appendix section we provide details on the velocity stencils, quadrature weights and speed of sound in the lattice  $c_s$ , used to implement the high order LBM models used in simulations in the main text. For the sake of completeness, we also provide details for the single-speed D2Q9 lattice used in Sec. 4.4.

The information for the D2Q9 is provided in Tab. 4. Data for the multi-speed D2Q17 is given in Tab. 5, while in Tab. 6 we give the data for the D2Q37. In all tables, each row is associated to a different fully symmetric set of discrete velocities, where the following notation is implied: e.g.  $(1, 1) = \{(-1, -1), (-1, 1), (1, -1), (1, 1)\}$ .

In order to implement CBC for thermal LBM simulation in  $d = 3$  spatial dimensions one can make use e.g. of the D3Q39 and the D3Q103 stencils, for which details on quadrature data can be found in Ref. [35].

## References

- [1] G. Hedstrom, Nonreflecting boundary conditions for nonlinear hyperbolic systems, *Journal of Computational Physics* 30 (2) (1979) 222–237. doi:10.1016/0021-9991(79)90100-1.

- [2] K. W. Thompson, Time dependent boundary conditions for hyperbolic systems, *Journal of Computational Physics* 68 (1) (1987) 1–24. doi:10.1016/0021-9991(87)90041-6.
- [3] T. Poinso, S. Lele, Boundary conditions for direct simulations of compressible viscous flows, *Journal of Computational Physics* 101 (1) (1992) 104–129. doi:10.1016/0021-9991(92)90046-2.
- [4] J. W. Kim, D. J. Lee, Generalized characteristic boundary conditions for computational aerocoustics, *AIAA Journal* 38 (11) (2000) 2040–2049. doi:10.2514/2.891.
- [5] R. D. Sandberg, N. D. Sandham, Nonreflecting zonal characteristic boundary condition for direct numerical simulation of aerodynamic sound, *AIAA Journal* 44 (2) (2006) 402–405. doi:10.2514/1.19169.
- [6] S. Wu, J. Wang, Numerical tests of a modified full implicit continuous Eulerian (FICE) scheme with projected normal characteristic boundary conditions for MHD flows, *Computer Methods in Applied Mechanics and Engineering* 64 (1-3) (1987) 267–282. doi:10.1016/0045-7825(87)90043-0.
- [7] A. Cimino, G. Krause, S. Elaskar, A. Costa, Characteristic boundary conditions for magnetohydrodynamics: The Brio–Wu shock tube, *Computers & Fluids* 127 (2016) 194–210. doi:10.1016/j.compfluid.2016.01.001.
- [8] C. S. Yoo, H. G. Im, Characteristic boundary conditions for simulations of compressible reacting flows with multi-dimensional, viscous and reaction effects, *Combustion Theory and Modelling* 11 (2) (2007) 259–286. doi:10.1080/13647830600898995.
- [9] C. S. Yoo, Y. Wang, A. Trouvé, H. G. Im, Characteristic boundary conditions for direct simulations of turbulent counterflow flames, *Combustion Theory and Modelling* 9 (4) (2005) 617–646. doi:10.1080/13647830500307378.
- [10] G. Lodato, P. Domingo, L. Vervisch, Three-dimensional boundary conditions for direct and large-eddy simulation of compressible viscous flows, *Journal of Computational Physics* 227 (10) (2008) 5105–5143. doi:10.1016/j.jcp.2008.01.038.
- [11] X. Shan, X.-F. Yuan, H. Chen, Kinetic theory representation of hydrodynamics: a way beyond the Navier-Stokes equation, *Journal of Fluid Mechanics* 550 (2006) 413–441. doi:10.1017/S0022112005008153.
- [12] D. A. Perumal, A. K. Dass, A review on the development of lattice Boltzmann computation of macro fluid flows and heat transfer, *Alexandria Engineering Journal* 54 (4) (2015) 955–971. doi:10.1016/j.aej.2015.07.015.
- [13] E. Calore, A. Gabbana, J. Kraus, E. Pellegrini, S. Schifano, R. Tripicione, Massively parallel lattice–Boltzmann codes on large GPU clusters, *Parallel Computing* 58 (2016) 1–24. doi:10.1016/j.parco.2016.08.005.
- [14] M. Bauer, S. Eibl, C. Godenschwager, N. Kohl, M. Kuron, C. Rettinger, F. Schornbaum, C. Schwarzmeier, D. Thönnies, H. Köstler, U. Rüde, walberla: A block-structured high-performance framework for multiphysics simulations, *Computers & Mathematics with Applications* 81 (2021) 478–501, development and Application of Open-source Software for Problems with Numerical PDEs. doi:10.1016/j.camwa.2020.01.007.
- [15] J. Latt, C. Coreixas, J. Beny, Cross-platform programming model for many-core lattice boltzmann simulations, *PLOS ONE* 16 (4) (2021) 1–29. doi:10.1371/journal.pone.0250306.
- [16] Z. Guo, T. S. Zhao, Lattice Boltzmann model for incompressible flows through porous media, *Phys. Rev. E* 66 (2002) 036304. doi:10.1103/PhysRevE.66.036304.
- [17] L. Chen, Q. Kang, Y. Mu, Y.-L. He, W.-Q. Tao, A critical review of the pseudopotential multiphase lattice Boltzmann model: Methods and applications, *International Journal of Heat and Mass Transfer* 76 (2014) 210–236. doi:10.1016/j.ijheatmasstransfer.2014.04.032.
- [18] N. S. Martys, H. Chen, Simulation of multicomponent fluids in complex three-dimensional geometries by the lattice Boltzmann method, *Physical Review E* 53 (1) (1996) 743–750. doi:10.1103/physreve.53.743.
- [19] P. Lallemand, L.-S. Luo, Hybrid Finite-Difference thermal Lattice Boltzmann Equation, *International Journal of Modern Physics B* 17 (01n02) (2003) 41–47. doi:10.1142/s0217979203017060.
- [20] Q. Li, K. H. Luo, Y. L. He, Y. J. Gao, W. Q. Tao, Coupling lattice Boltzmann model for simulation of thermal flows on standard lattices, *Physical Review E* 85 (1) (Jan. 2012). doi:10.1103/physreve.85.016710.
- [21] X. Shan, General solution of lattices for Cartesian lattice Bhatnagar-Gross-Krook models, *Phys. Rev. E* 81 (2010) 036702. doi:10.1103/PhysRevE.81.036702.
- [22] P. C. Philippi, L. A. Hegele, L. O. E. dos Santos, R. Surmas, From the continuous to the lattice Boltzmann equation: The discretization problem and thermal models, *Physical Review E* 73 (5) (may 2006). doi:10.1103/physreve.73.056702.
- [23] A. Scagliarini, L. Biferale, M. Sbragaglia, K. Sugiyama, F. Toschi, Lattice Boltzmann methods for thermal flows: Continuum limit and applications to compressible Rayleigh-Taylor systems, *Physics of Fluids* 22 (5) (2010) 055101. doi:10.1063/1.3392774.
- [24] S. Izquierdo, N. Fueyo, Characteristic nonreflecting boundary conditions for open boundaries in lattice Boltzmann methods, *Physical Review E* 78 (4) (Oct. 2008). doi:10.1103/physreve.78.046707.
- [25] K. Dehee, K. H. Min, S. M. Jhon, J. S. Vinay, B. John, A characteristic non-reflecting boundary treatment in lattice Boltzmann method, *Chinese Physics Letters* 25 (6) (2008) 1964–1967. doi:10.1088/0256-307x/25/6/012.
- [26] D. Heubes, A. Bartel, M. Ehrhardt, Characteristic boundary conditions in the lattice Boltzmann method for fluid and gas dynamics, *Journal of Computational and Applied Mathematics* 262 (2014) 51–61. doi:10.1016/j.cam.2013.09.019.
- [27] N. Jung, H. W. Seo, C. S. Yoo, Two-dimensional characteristic boundary conditions for open boundaries in the lattice Boltzmann methods, *Journal of Computational Physics* 302 (2015) 191–199. doi:10.1016/j.jcp.2015.08.044.
- [28] G. Wissocq, N. Gourdain, O. Malaspinas, A. Eyssartier, Regularized characteristic boundary conditions for the Lattice-Boltzmann methods at high Reynolds number flows, *Journal of Computational Physics* 331 (2017) 1–18. doi:10.1016/j.jcp.2016.11.037.
- [29] J. Jacob, P. Sagaut, Solid wall and open boundary conditions in hybrid recursive regularized lattice Boltzmann method for compressible flows, *Physics of Fluids* 31 (12) (2019) 126103. doi:10.1063/1.5129138.
- [30] T. Gianoli, J.-F. Boussuge, P. Sagaut, J. de Laborderie, Development and validation of Navier–Stokes characteristic boundary conditions applied to turbomachinery simulations using the lattice Boltzmann method, *International Journal for Numerical Methods in Fluids* 95 (4) (2022) 528–556. doi:10.1002/flid.5160.
- [31] F. Klass, A. Gabbana, A. Bartel, A characteristic boundary condition for multispeed lattice Boltzmann methods, *Communications in Computational Physics* 33 (1) (2023) 101–117. doi:10.4208/cicp.oa-2022-0052.
- [32] X. Chen, K. Yang, X. Shan, Characteristic boundary condition for multispeed lattice Boltzmann model in acoustic problems, *Journal of Computational Physics* (2023) 112302. doi:10.1016/j.jcp.2023.112302.
- [33] T. Krüger, H. Kusumaatmaja, A. Kuzmin, O. Shardt, G. Silva, E. M. Viggen, *The Lattice Boltzmann Method*, Springer International Publishing, 2017. doi:10.1007/978-3-319-44649-3.
- [34] S. Succi, *The Lattice Boltzmann Equation: For Complex States of Flowing Matter*, OUP Oxford, 2018. doi:10.1093/oso/9780199592357.001.0001.
- [35] X. Shan, The mathematical structure of the lattices of the lattice Boltzmann method, *Journal of Computational Science* 17 (2016) 475–481. doi:10.1016/j.jocs.2016.03.002.
- [36] P. L. Bhatnagar, E. P. Gross, M. Krook, A Model for Collision Processes in Gases. Amplitude Processes in Charged and Neutral One-Component Systems, *Phys. Rev.* 94 (3) (1954) 511–525. doi:10.1103/PhysRev.94.511.
- [37] S. Chapman, T. G. Cowling, *The Mathematical Theory of Non-Uniform Gases*, 3rd ed, Cambridge University Press, 197. doi:10.1119/1.1942035.

